Spiral modes supported by circular dielectric tubes and tube segments

Lena Ebers, Manfred Hammer, Jens Förstner*
Theoretical Electrical Engineering, Paderborn University, Paderborn, Germany

Abstract: The modal properties of curved dielectric slab waveguides are investigated. We consider quasi-confined, attenuated modes that propagate at oblique angles with respect to the axis through the center of curvature. Our analytical model describes the transition from scalar 2-D TE/TM bend modes to lossless spiral waves at near-axis propagation angles, with a continuum of vectorial attenuated spiral modes in between. Modal solutions are characterized in terms of directional wavenumbers and attenuation constants. Examples for vectorial mode profiles illustrate the effects of oblique wave propagation along the curved slab segments. For the regime of lossless spiral waves, the relation with the guided modes of corresponding dielectric tubes is demonstrated.

Keywords: integrated optics, bent slab waveguides, oblique propagation, bend modes, tube modes, spiral waves, numerical/analytical modeling.

1 Introduction

Bends in dielectric optical waveguides are basic building blocks for various kinds of integrated photonic circuitry. The accurate evaluation of modal propagation and attenuation constants, and of modal electromagnetic field profiles, constitutes the essential theoretical task. Just as for straight waveguides, modal analysis of general 3-D bend channels is possible only by numerical means. The fundamental phenomena related to the waveguide curvature, however, can be studied conveniently by looking at analytical 2-D models [1, 2] of bent slab waveguides with 1-D cross sections. These bent slab models correspond to physical configurations, where both the structure under investigation and the electromagnetic field are constant along the axis through the center of the curved structure. The solutions are quasi-guided attenuated waves that propagate along the curved slab, in a direction perpendicular to the axis.

In this paper we reconsider the bent slab structures, but now look at quasi-guided waves that also have an axial wavenumber component. Referring to the cylindrical coordinate system (r, θ, y) of Figure 1, these modes propagate in a direction given by the azimuthal θ- and axial y-propagation constants, with profiles that are quasi-confined in the radial r-direction. The curves given by these local wavenumbers describe spirals around the central axis, hence we call these fields "spiral modes".

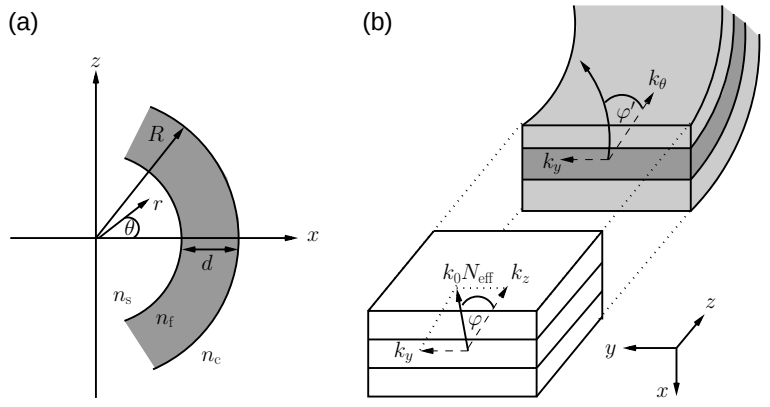

Figure 1: (a) Bent slab waveguide with outer radius R, thickness d and refractive indices n_s, n_f and n_c in the interior, film, and exterior regions. Cylindrical coordinates r, θ, and y complement the Cartesian x-y-z coordinates. The structure is constant along the y- and θ-axes. (b) Imagined excitation of the bent waveguide segment by a semi-guided plane wave, propagating in the straight region at angle φ with wavenumbers k_y and k_z. In the curved region, this leads to a spiral wave with wavenumbers k_y and k_θ, propagating at an angle φ' .

Besides the — for the most part academic — interest in these fields, the present study was motivated mainly by our recent results on oblique waves in segmented slab waveguides [3] and dielectric steps [4, 5], which adopt quite early concepts of integrated optics [6, 7]. One considers semi-guided, laterally plane waves supported by a piece of slab waveguide, and the oblique incidence of such waves on nonuniformities in the slab. These need to be constant along one axis, and can otherwise be of arbitrary shape. Examples are linear boundaries

* *University of Paderborn, FG Theoretical Electrical Engineering Warburger Str. 100, 33098 Paderborn, Germany*
Phone: ++49(0)5251/60-3560 Fax: ++49(0)5251/60-3524 E-mail: manfred.hammer@uni-paderborn.de

between slab regions of different thicknesses [3], or more involved linear corner-, step-, or even bridge- or u-turn-like structures [5]. A critical angle of incidence can be identified, beyond which power transfer to non-guided, radiative waves is forbidden. Depending on the particular geometry, oblique waves at higher angles of incidence are partly reflected and partly transmitted, without any radiation losses.

In this context, as hinted at in Figure 1(b), one might consider a segment of a dielectric tube as a specific form of a slab waveguide nonuniformity. The entire system is constant along the axis of curvature, here the y-direction. A semi-guided wave, supported by the straight slab, and coming in at the interface with a specific angle of incidence φ, requires a solution in the tube segment with a y-wavenumber k_y that matches that of the incoming wave. Note that here the particularities concerning the transition from the straight to the curved sections are irrelevant; we do not look at the transition itself in this paper.

Still, when imagining a variation of this angle of incidence φ, translated to a variation of the wavenumber parameter k_y, one expects different scenarios. For normal incidence $\varphi = 0$, the familiar 2-D bend modes will be exited in the tube segment, with fields that are constant along y. For near-grazing incidence, at φ close to 90°, lossless waves can be expected that, for specific angles, and envisioning a continuation of the curved segment to a complete dielectric tube, form the guided modes supported by this tube-shaped optical fiber. In between, there is a continuum of vectorial waves, that spiral around the tube axis at varying angles, with varying levels of radiative losses that vanish beyond a certain critical angle of incidence. The full range of solutions will be explored in this paper, where we (mostly) look at angular segments of curved slabs only, disregarding any potential resonant properties.

Section 2 provides a detailed analysis of the vector spiral modes. Exploiting the facilities for Bessel- and Hankel functions with complex order and argument built into the *Maple* computer algebra system [8], the results are almost fully analytic. Besides the numerical solution of transcendental equations, no further approximations enter. Section 3 summarizes results for a series of configurations with different levels of refractive index contrast.

Spiral waves supported by infinite circular dielectric rods / circular fibers have been investigated both theoretically [9, 10, 11] and experimentally [12], with emphasis on resonant features (also as a means to approximate the whispering gallery resonances of dielectric disks of finite thickness [9]), on far-field properties [11], and considering excitation by external free-space plane waves, or by external focused Gaussian beams. These excitation and readout schemes cannot reach spiral waves with parameters k_y beyond the free space wavenumber of the external medium, i.e. cannot reach the lossless spiral waves at high propagation angles (These should become accessible through evanescent excitation by another waveguide [13], though). We shall see that there is a smooth transition from lossy bend modes to lesser-attenuated spiral modes to lossless spiral waves that constitute the guided modes of a dielectric tube. Note that most of our formalism, with small modifications, applies to rod configurations ($n_\mathrm{s} = n_\mathrm{f}$) as well.

2 Theory

Figure 1(a) shows a curved slab waveguide with one inner layer. All regions are made of linear dielectric, nonmagnetic, lossless, and isotropic material, with constant refractive indices $n_\mathrm{s}, n_\mathrm{f}$, and n_c, in the interior, film, and exterior regions, where we assume $n_\mathrm{s} \leq n_\mathrm{f} > n_\mathrm{c}$. The waveguide is regularly bent around the y-axis with outer radius R and thickness d. Because of this symmetry we adopt cylindrical coordinates r, θ, y, as introduced in the figure. The structure is homogeneous along the angular coordinate θ.

The homogeneous Maxwells equations in the frequency domain [14] apply, here written for a time dependence $\sim \exp(\mathrm{i}\omega t)$ of all fields, with the angular frequency $\omega = k_0 \mathrm{c} = 2\pi \mathrm{c}/\lambda$ specified by the vacuum wavenumber k_0, or wavelength λ, respectively, for vacuum speed of light c, vacuum permittivity ϵ_0 and permeability μ_0:

$$\mathrm{curl}\, \tilde{\boldsymbol{E}} = -\mathrm{i}\omega\mu_0 \tilde{\boldsymbol{H}}, \qquad \mathrm{curl}\, \tilde{\boldsymbol{H}} = \mathrm{i}\omega\epsilon_0\epsilon \tilde{\boldsymbol{E}}. \tag{1}$$

Local refractive indices n define the relative permittivity $\epsilon = n^2$.

2.1 Oblique wave propagation along bent slab waveguides

Interest is in optical electric and magnetic fields $\tilde{\boldsymbol{E}}$, $\tilde{\boldsymbol{H}}$ that vary harmonically along y with wavenumber k_y, with — at present unknown — cross sectional mode profiles $\boldsymbol{E}$ and $\boldsymbol{H}$:

$$\tilde{\boldsymbol{E}}(r,\theta,y) = \boldsymbol{E}(r,\theta)\,\mathrm{e}^{-\mathrm{i}k_y y}, \quad \tilde{\boldsymbol{H}}(r,\theta,y) = \boldsymbol{H}(r,\theta)\,\mathrm{e}^{-\mathrm{i}k_y y}. \tag{2}$$

In the present context, k_y is a given parameter. To render its values more accessible, we adopt the viewpoint of external excitation of the field in the bend slab, as illustrated in Figure 1(b). Connection of a field supported by the straight waveguide to the solution in the curved one requires that both share the same y-wavenumber [3]. A semi-guided plane wave in the straight region, with effective mode index N_{eff}, is associated with a dependence $\exp(-\mathrm{i}k_y y)$, where $k_y = k_0 N_{\text{eff}} \sin\varphi$ is then given by the angle of incidence φ of the wave with respect to the propagation in the y-z-plane. Envisioning a direct linear joint between the straight and the bent waveguide segments, it appears appropriate (and we will do so throughout this paper) to apply the layering of the bend also in the straight segment. Then N_{eff} is the effective mode index of the — polarized — guided mode of the straight slab waveguide of thickness d with refractive index profile $n_{\text{s}} : n_{\text{f}} : n_{\text{c}}$ at the relevant vacuum wavelength. We shall see below that this choice also renders φ close to the actual propagation angle φ' of the spiral mode inside the bend.[1] By varying $\varphi \in [0, 90[^\circ$, a range of wavenumbers $k_y \in [0, k_0 N_{\text{eff}}[$ can be scanned.

We are left with the task to determine the electric and magnetic parts $\boldsymbol{E}$, $\boldsymbol{H}$ of the modal field. By inserting the ansatz Eq. (2) into the governing Maxwell equations (1), we obtain the coupled equations

$$\begin{gathered}\frac{1}{r}\partial_\theta E_y + \mathrm{i}k_y E_\theta = -\mathrm{i}\omega\mu_0 H_r, \quad -\mathrm{i}k_y E_r - \partial_r E_y = -\mathrm{i}\omega\mu_0 H_\theta, \quad \frac{1}{r}\partial_r(rE_\theta) - \frac{1}{r}\partial_\theta E_r = -\mathrm{i}\omega\mu_0 H_y, \\ \frac{1}{r}\partial_\theta H_y + \mathrm{i}k_y H_\theta = \mathrm{i}\omega\epsilon_0\epsilon E_r, \quad -\mathrm{i}k_y H_r - \partial_r H_y = \mathrm{i}\omega\epsilon_0\epsilon E_\theta, \quad \frac{1}{r}\partial_r(rH_\theta) - \frac{1}{r}\partial_\theta H_r = \mathrm{i}\omega\epsilon_0\epsilon E_y.\end{gathered} \tag{3}$$

Restricting, for the moment, to positions with locally constant permittivity, Eqs. (3) can be combined into the scalar second order equations

$$\partial_r^2\psi + \frac{1}{r}\partial_r\psi + \frac{1}{r^2}\partial_\theta^2\psi + (k_0^2\epsilon - k_y^2)\psi = 0, \tag{4}$$

which hold for $\psi = E_y$ and $\psi = H_y$ in regions with constant refractive index. Once solutions for these principal components are at hand, the other components can be calculated as

$$\begin{aligned} E_r &= -\frac{\mathrm{i}}{k_0^2\epsilon - k_y^2}\Big(k_y\partial_r E_y + \frac{\omega\mu_0}{r}\partial_\theta H_y\Big), \quad E_\theta = -\frac{\mathrm{i}}{k_0^2\epsilon - k_y^2}\Big(\frac{k_y}{r}\partial_\theta E_y - \omega\mu_0\partial_r H_y\Big), \\ H_r &= -\frac{\mathrm{i}}{k_0^2\epsilon - k_y^2}\Big(k_y\partial_r H_y - \frac{\omega\epsilon_0\epsilon}{r}\partial_\theta E_y\Big), \quad H_\theta = -\frac{\mathrm{i}}{k_0^2\epsilon - k_y^2}\Big(\frac{k_y}{r}\partial_\theta H_y + \omega\epsilon_0\epsilon\partial_r E_y\Big). \end{aligned} \tag{5}$$

2.1.1 Separable principal components

Local solutions of Eq. (4) are obtained by writing the principal fields in separable form $\psi(r,\theta) = f(r)\,g(\theta)$. Then Eq. (4) leads to the two equations

$$g'' + \alpha g = 0 \qquad \text{and} \qquad r^2 f'' + r f' + (r^2\chi^2 - \alpha) f = 0, \tag{6}$$

for the radial and angular functions f, g, where the dashes denote derivatives, $\alpha \in \mathbb{C}$ is a constant, and $\chi^2 = k_0^2 n^2 - k_y^2$. Eq. (6) holds within regions with constant refractive index n.

Introducing the — at present unknown — angular mode order ν and angular propagation constant k_θ by $\alpha = \nu^2$ and $\nu = k_\theta R$, a solution g of Eq. (6) is readily written as[2]

$$g(\theta) \sim \mathrm{e}^{-\mathrm{i}\sqrt{\alpha}\theta} = \mathrm{e}^{-\mathrm{i}k_\theta R\theta}. \tag{7}$$

[1] Other scenarios, like the evanescent excitation through a slab, with potentially different layering, placed "underneath" the bend at a small distance, would lead to a different rule of translating k_y to an angle of incidence.

[2] Note that the definition of k_θ depends on the — arbitrary — definition of the bend radius R [2].

We are interested in waves that propagate and decay in positive θ-direction. Therefore only values k_θ with positive real part and negative imaginary part are relevant here.

By now it is possible to define a propagation angle φ' in the bent waveguide structure through the relation $\tan\varphi' = k_y/\Re\, k_\theta$. Note that, in general, φ' differs from φ due to differing guidance properties of the bend and straight slabs (even for identical layering).

We proceed with the equation for the radial function f, where a case distinction is required, depending on the local refractive index value n. For $k_0 n > k_y$, Eq. (6) is a standard Bessel differential equation, and its elementary solutions are Bessel functions of the first kind J and of the second kind Y [15]. For $k_0 n < k_y$, the negative value for $\chi^2 = k_0^2 n^2 - k_y^2$ leads to a differential equation of modified Bessel type. Elementary solutions are the modified Bessel functions of the first kind I and the second kind K [15], which can be expressed through the Bessel functions J and the Hankel function $\mathrm{H}^{(2)}$.

We are looking for spiral modes that are regular at the central axis $r = 0$ of the cylindrical coordinates, and that relate to outwards traveling, or externally decaying, waves at large radial coordinates. These physical boundary conditions are implemented by selecting appropriate elementary solutions, separately for the radial intervals with constant refractive index. Considering the interior region with refractive index n_s, the fields should be regular at $r = 0$. So in case of $k_0 n_\mathrm{s} > k_y$, the ansatz needs to be restricted to the Bessel function of the first kind J, while for $k_0 n_\mathrm{s} < k_y$ the modified Bessel function of first kind I would be appropriate. Because of the proportionality $\mathrm{I}(x) \sim \mathrm{J}(\mathrm{i}x)$, we can write the solution in terms of the Bessel function J in both cases. Next looking at the core layer with $n = n_\mathrm{f}$, the general solution for $f(r)$ is given by a linear combination of the Bessel functions J and Y. Assuming a core layer with the highest local refractive index $n_\mathrm{f} \geq n_\mathrm{s}, n_\mathrm{c}$, such that $k_0 n_\mathrm{f} \geq k_y = k_0 N_\mathrm{eff} \sin\varphi$, here a further differentiation is not necessary. Outside the core, for $r > R$, we need to restrict to outgoing and/or decaying fields. In case of $k_0 n_\mathrm{c} > k_y$, these are realized by a specific complex linear combination of J and Y, i.e. by the Hankel function $\mathrm{H}^{(2)}$, as can be verified by inspecting the asymptotic expansion of $\mathrm{H}^{(2)}$ for large arguments [15, 2]. For $k_0 n_\mathrm{c} < k_y$, the modified Bessel functions K can also be replaced by the Hankel function $\mathrm{H}^{(2)}$, with negative, imaginary argument, to represent (outgoing) decaying waves.

For the sake of clarity, we now specialize to "symmetric" configurations with equal refractive indices $n_\mathrm{s} = n_\mathrm{c}$ in the interior and exterior regions, with a core layer of higher refractive index n_f in-between. These will be selected as examples in Section 3. A global ansatz for the principal fields $\psi = E_y$ and $\psi = H_y$ can be stated as

$$\psi(r,\theta) = \begin{cases} A\,\mathrm{J}_\nu(r\sqrt{k_0^2 n_\mathrm{s}^2 - k_y^2})\,\mathrm{e}^{-\mathrm{i}\nu\theta}, & \text{for } 0 \leq r \leq R-d, \\ \left(B\,\mathrm{J}_\nu(r\sqrt{k_0^2 n_\mathrm{f}^2 - k_y^2}) + C\,\mathrm{Y}_\nu(r\sqrt{k_0^2 n_\mathrm{f}^2 - k_y^2})\right)\mathrm{e}^{-\mathrm{i}\nu\theta}, & \text{for } R-d \leq r \leq R, \\ D\,\mathrm{H}_\nu^{(2)}(\pm r\sqrt{k_0^2 n_\mathrm{c}^2 - k_y^2})\,\mathrm{e}^{-\mathrm{i}\nu\theta}, & \text{for } r \geq R, \end{cases} \tag{8}$$

with Bessel- and Hankel-functions of — in general — complex order $\nu = k_\theta R$, and either real or imaginary arguments. In the third case, the $\pm$-sign applies for parameters $k_y \lessgtr k_0 n_\mathrm{c}$. Note that separate expressions (8) need to be written for E_y and H_y, with separate coefficients A, B, C, and D.

2.1.2 Transverse resonance

Using the relations (5), Eqs. (8) for the principal components can be extended towards expressions for the full vectorial electromagnetic mode profile, including the in total eight unknown amplitudes, and depending on the still unknown angular wavenumber k_θ. These fields satisfy the Maxwell equations (1) everywhere, with the exception of the interfaces at $r = R$ and $r = R - d$. Standard expressions for the continuity of electromagnetic fields at uncharged dielectric interfaces apply [14]. With the present cylindrical coordinates, continuity of the tangential electric field components E_y, E_θ, of all magnetic field components H_y, H_θ, and H_r, and of the normal component $\sim \epsilon E_r$ of the dielectric displacement is required at $r = R$ and $r = R - d$.

Taking into account redundancy, these interface conditions lead to a system of eight linear equations for the local amplitudes. For purposes of reference, explicit expressions are given in Appendix A. These equations can be written in the form of a nonlinear eigenvalue equation

$$\mathsf{M}(k_\theta)\mathbf{A} = 0, \tag{9}$$

where the matrix M depends on the unknown wavenumber k_θ, and where the vector $\mathbf{A}$ collects the eight amplitudes $\{A, \ldots, D\}_{E,H}$ introduced in Eq. (8). Interest is in nonzero solutions of Eq. (9). Valid angular wavenumbers are thus found by identifying values k_θ where $\mathsf{M}(k_\theta)$ becomes singular, i.e. where the determinant of that matrix vanishes. That condition represents the "transverse resonance condition" of the present spiral modes. Note that, in general, Eq. (9) leads to vectorial solutions in the form (2), where all six electromagnetic mode profile components are nonzero.

2.1.3 Computational procedure

The transverse resonance condition for the spiral modes does not permit an analytical solution. Roots k_θ of the transcendental equation $\det(\mathbf{M}(k_\theta)) = 0$ associated with Eq. (9) need to be found in the complex plane, where, for physical reasons as given above, we can restrict to the quadrant $\Re\, k_\theta > 0$, $\Im\, k_\theta < 0$. The complex secant method [16] was implemented in the *Maple* computer algebra system [8]. For the present equations, the routine usually converges rapidly to the root positions, provided that a good initial guess is available for each individual configuration. We thus applied a procedure to trace solutions for structures with close parameters in the complex plane.

In the limit of vanishing curvature, one expects that the waveguiding properties of the present bent slabs become those of straight slab waveguides with equivalent layering. Given a value k_y, or an angle φ, respectively, the wavenumber component $k_z = k_0 N_{\text{eff}} \cos(\varphi)$ associated with the oblique propagation (cf. Figure 1) in the straight slab, together with an additional small imaginary part, can serve as a suitable initial guess when searching for eigenvalues k_θ of a bend configuration with "large" radius R. Solutions for stronger curvature are found by proceeding along a series of decreasing radii, always using the root of the preceding step as initial guess for the configurations with the next smaller radius.

2.2 Scalar 2-D bend modes

A vanishing axial wavenumber parameter $k_y = 0$ relates to fields (2) that are constant along the y-axis. Accepting the above viewpoint of excitation through a straight slab waveguide, this corresponds to a case of normal incidence $\varphi = 0$ of the incoming semi-guided wave. Eqs. (3) then split into the two separate sets

$$\frac{1}{r}\partial_\theta E_y = -\mathrm{i}\omega\mu_0 H_r, \quad -\partial_r E_y = -\mathrm{i}\omega\mu_0 H_\theta, \quad \frac{1}{r}\partial_r(rH_\theta) - \frac{1}{r}\partial_\theta H_r = \mathrm{i}\omega\epsilon_0\epsilon E_y, \tag{10}$$

and

$$\frac{1}{r}\partial_\theta H_y = \mathrm{i}\omega\epsilon_0\epsilon E_r, \quad -\partial_r H_y = \mathrm{i}\omega\epsilon_0\epsilon E_\theta, \quad \frac{1}{r}\partial_r(rE_\theta) - \frac{1}{r}\partial_\theta E_r = -\mathrm{i}\omega\mu_0 H_y. \tag{11}$$

of equations for the modes of 2-D bent slab waveguides [1, 2]. Solutions for transverse electric (TE-) bend modes with nonzero E_y, H_r, and H_θ fields can be found by considering a scalar problem for their principal E_y component. Transverse electric (TM-) bend modes with nonzero H_y, E_r, and E_θ components are characterized through a scalar equation for the principal component H_y. Our present formalism covers these cases as well; respective results from Ref. [2] will serve as benchmarks.

2.3 Guided modes of full dielectric tubes

Following the reasoning of Ref. [5], and accepting the curved segment as a particular kind of linear "nonuniformity" in an otherwise straight slab, one concludes that any radiative losses caused by the curvature vanish, if only the axial wavenumber k_y is larger than the wavenumber $k_0 n_\mathrm{c}$ of plane waves in the exterior region. In the present setting, this translates to a critical angle of incidence $\tilde{\varphi}$ with $\sin\tilde{\varphi} = n_\mathrm{c}/N_{\text{eff}}$. Spiral modes that relate to incoming waves at angles $\varphi > \tilde{\varphi}$, i.e. that correspond to axial wavenumbers $k_y = k_0 N_{\text{eff}} \sin\varphi > k_0 n_\mathrm{c}$, are lossless. In our previous formalism, this can be realized by inspecting the ansatz (8) for the principal mode components: In the expression for the exterior region $r > R$, the argument of $\mathrm{H}_\nu^{(2)}$ switches from real to imaginary, and the behaviour of the profile components changes from oscillatory to decaying, at $k_y = k_0 n_\mathrm{c}$.

Consequently, for large k_y with $\varphi > \tilde{\varphi}$, *real* eigenvalues k_θ are expected as solutions of Eq. (9). In case these happen to coincide with an integer angular order $\nu = k_\theta R \in \mathbb{Z}$, the respective spiral mode fields can be continued to establish valid confined solutions of Eqs. (1) for an entire dielectric tube (cf. Figure 1 & Eq. (7)).

We are thus led to the guided modes of circular dielectric fibers [17, 18], here with specific single-layer step-index profiles. Owing to their resemblance to a dielectric tube, these solutions will be called "tube modes" in the following sections.

When trying to identify these tube modes directly, the previous formalism can advantageously be reformulated by exchanging the roles of k_y and k_θ. An integer angular order $\nu = k_\theta R$ is selected as a given parameter, and k_y takes the role of the unknown eigenvalue (the matrix M in Eq. (9) is regarded as a function of k_y). Propagation constants k_y of the tube modes are then searched on the real axis only, in the interval $k_0 n_\mathrm{c} < k_y < k_0 n_\mathrm{f}$. One thus recovers a standard guided wave eigenvalue problem. Respective comparisons will serve for further benchmarks. Note that the tube modes are each twofold degenerate: Any eigenvalue k_y corresponds to two solutions for $\pm\nu$ with opposite sense of rotation (rotational symmetry; ν appears merely quadratically in Eq. (6); an ansatz in terms of $\sin$ and $\cos$-functions could alternatively be chosen for the angular function g in Eq. (7)).

3 Examples

Table 1 collects structural and material parameters for the examples discussed in this section. A first set of values concerns waveguides with low / moderate refractive contrast. Respective bend configurations have been investigated in Ref. [2], such that a direct validation of our results for $\varphi = 0$ is possible. These waveguide bends are comparably lossy, such that the vanishing of losses at larger angles of propagation can be highlighted. However, any effects related to the vectorial character of the spiral modes at $\varphi > 0$ should become more pronounced for higher refractive index contrast. We therefore adopt a second set of parameters, with a thinner core layer. In the following sections we refer to these settings as "low" and "high refractive index contrast", or with the shorthands "(lc)" and "(hc)", implying that the associated different core layer thicknesses are applied. In both cases, the respective straight slab waveguides are single mode, per polarization. The effective indices N_eff of the polarized fundamental TE_0 and TM_0 slab modes, determined by the solver of Ref. [19], will be used to characterize the k_y parameter for the spiral mode analysis.

	n_s	n_f	n_c	$d/\,\mu$m	$\lambda/\,\mu$m	R, φ	
(lc)	1.6	1.7	1.6	1.0	1.3	varied	[2]
(hc)	1.5	2.0	1.5	0.4	1.3	varied	

Table 1: Parameters for the examples with lower (lc) and higher contrast (hc) in Sections 3.1 – 3.3. Bend slab waveguides as in Figure 1 are considered, with refractive indices n_s, n_c, and n_f, core thickness d, at vacuum wavelength λ, for varying bend radius R and propagation angle φ.

Our computational procedure (cf. Section 2.1.3) establishes a link between any particular spiral mode, and the polarized slab waveguide mode, the effective index N_eff of which served as initial guess for the root-tracing steps that led to the spiral mode solution. For lack of any better naming scheme, we thus adopt the terms "TE / TM" also for the vectorial spiral modes identified in this way. The findings on the polarization character of the hybrid spiral modes in Section 3.2 prove this scheme to be adequate.

3.1 Bend modes

We start with a brief look at "conventional" 2-D bend mode configurations. As discussed in Section 2.2, for $k_y = 0$, $\varphi = 0$, separate scalar equations determine the familiar TE- and TM-polarized modes of bent slab waveguides. Figure 2 shows propagation and attenuation constants of polarized bend modes for the settings with low and high refractive index contrast. Figure 3 illustrates a series of bend mode profiles.

According to Figure 2, for low curvature bends, the effective indices $\Re\, k_\theta/k_0$ of the bend modes approach the levels of their straight waveguide counterparts, while the attenuation constants $\Im\, k_\theta$ tend to zero for large bend radii R. More pronounced deviations in wavenumbers, and larger levels of loss, are observed for stronger curvature at smaller radii R.[3] Coincidence of the present wavenumber values with the data from Ref. [2] validates this part of the theory and our implementation.

[3] Note that it depends on the (arbitrary) definition of the bend radius, whether, for large R, the curve $\Re\, k_\theta/k_0$ approaches the level N_eff from above, or from below [2].

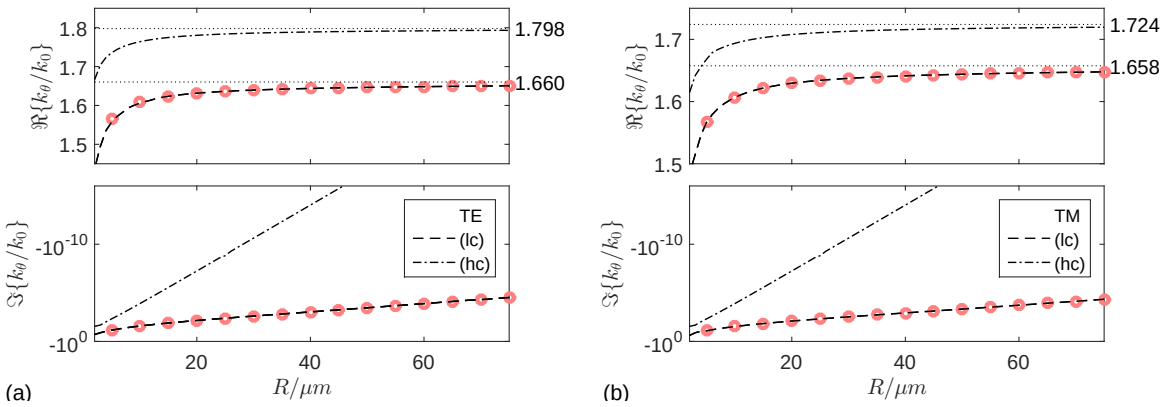

Figure 2: Wavenumbers k_θ, real (top) and imaginary parts (bottom) of bent slab waveguides, depending on the core radius R, for normal wave propagation $k_y = 0$, $\varphi = 0$. Results for TE- (a) and TM-polarization (b) are compared, for structures with low- and high contrast, as introduced in Table 1. The markers show reference data from [2]; horizontal lines indicate effective indices N_{eff} of the associated fundamental TE_0, TM_0 modes of straight waveguides [19].

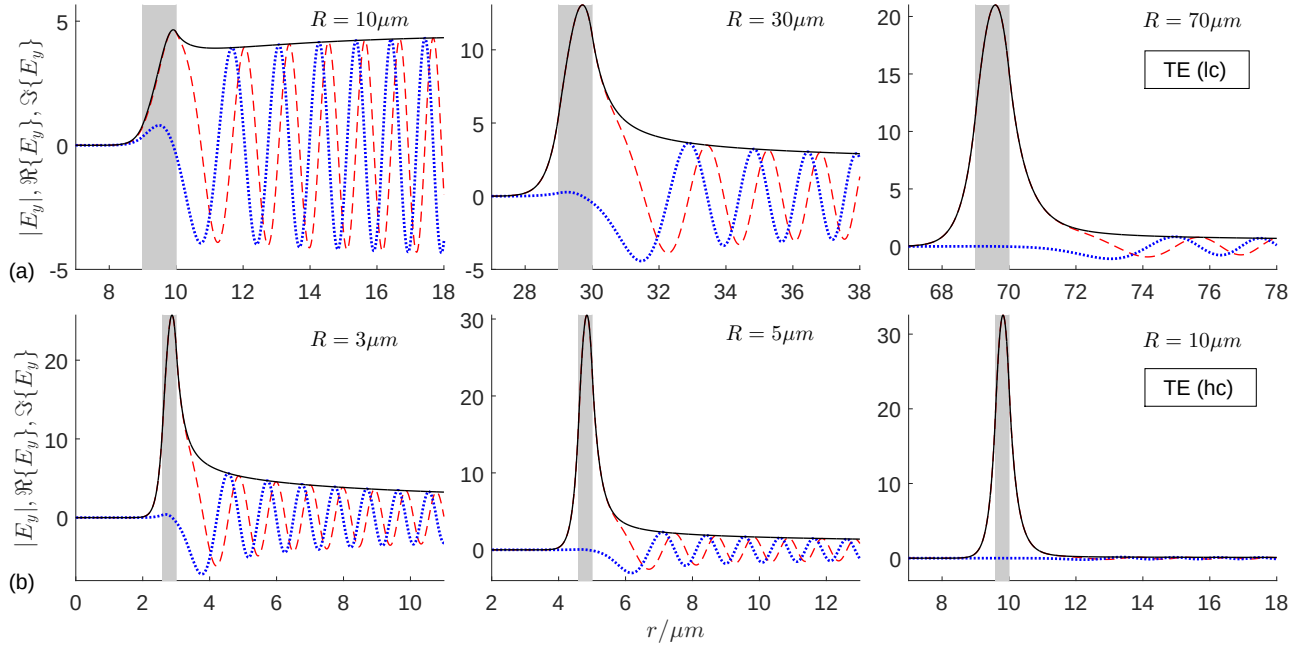

Figure 3: Radial profiles of TE-polarized bend modes, for different bend radii R, for 2-D bend waveguides ($k_y = 0$, $\varphi = 0$) with lower (a) and higher refractive index contrast (b); parameters as in Table 1. Curves for the absolute value $|E_y|$ (continuous), the real part $\Re\, E_y$ (dashed), and the imaginary part $\Im\, E_y$ (dotted) of the principal electric field component are shown. The gray patches indicate the positions of the waveguide cores.

Figure 3 shows principal field components of the TE bend modes, for different bend radii, and for the low and high refractive index contrast scenarios. The modes are normalized to unit power [2], using the expression

$$P_\theta = \frac{1}{2}\int_0^\infty \Re\{\boldsymbol{E} \times \boldsymbol{H}^*\} \cdot \boldsymbol{e}_\theta \, \mathrm{d}r \tag{12}$$

for the angular optical power flow per axial unit length, evaluated with fields (2), (8) at $\theta = 0$. Here $\boldsymbol{e}_\theta$ is a unit vector in the angular direction θ.

Radiative losses relate to mode profiles with pronounced oscillatory behaviour in the external region $r > R$. In line with Figure 2, the strength of these oscillations decreases, and confinement of the mode to the core region improves, with lower curvature at larger bend radii, and for stronger refractive index contrast. For the better confined modes with lower losses, one also finds a more symmetric profile with the absolute profile maximum close to the center of the core; the bend modes then resemble the symmetric modes of straight waveguides with the same layering.

3.2 Spiral modes

Accepting fixed layering and vacuum wavelength, two primary parameters determine the modal properties of the tube segment. These are the radius of curvature R and the axial wavenumber k_y, or the angle of incidence φ, respectively. Figures 4–7 summarize our results for the influence of these two parameters on the complex wavenumbers of spiral modes. In each of the figures, the wavenumber data is displayed twice: The left panels show the dependence of the radius R of curvature, for a number of different angles of incidence φ; attenuation constants are displayed on a logarithmic scale. The roles of R and φ are exchanged for the panels on the right hand side; here we have chosen a linear scale for the attenuation constants. All curves in these figures for $\varphi = 0$ coincide with the data of Figure 2.

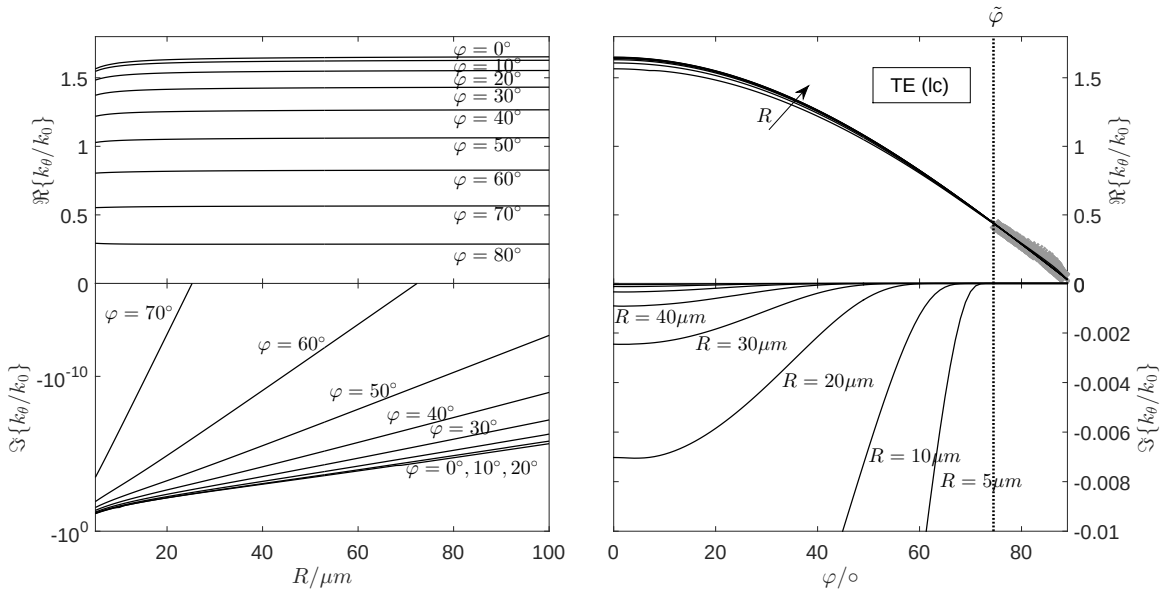

Figure 4: Spiral mode wavenumbers k_θ, real & imaginary parts, for low refractive index contrast (cf. Table 1) and TE-like fields, as a function of bend radius R and angle of incidence φ; critical angle $\tilde{\varphi} = 74.5°$. The markers in the region $\varphi > \tilde{\varphi}$ relate to tube modes, as discussed in Section 3.3 (see Figure 14).

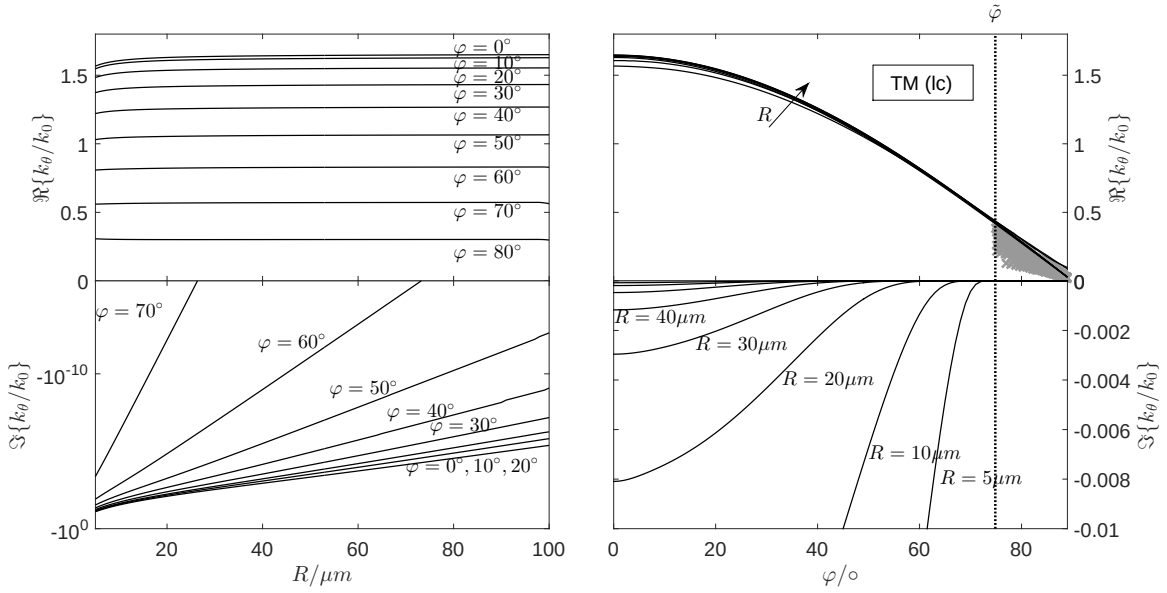

Figure 5: Spiral mode wavenumbers k_θ, real & imaginary parts, for low refractive index contrast (cf. Table 1) and TM-like fields, as a function of bend radius R and angle of incidence φ; critical angle $\tilde{\varphi} = 74.86°$.

First we look at the angular propagation constant $\Re\, k_\theta$ of the spiral modes, or their effective indices $\Re\, k_\theta/k_0$, respectively. In the limit of low curvature, for large bend radii, one expects an angular behaviour as for oblique wave propagation in a straight slab waveguide. For oblique propagation at angle φ, these waves with effective index N_{eff} propagate with a y-wavenumber $k_y = k_0 N_{\text{eff}} \sin\varphi$, such that a value $k_\theta \approx k_z = k_0 N_{\text{eff}} \cos\varphi$ can be expected for the angular propagation constant (see Figure 1). This explains the limiting levels in the left panels

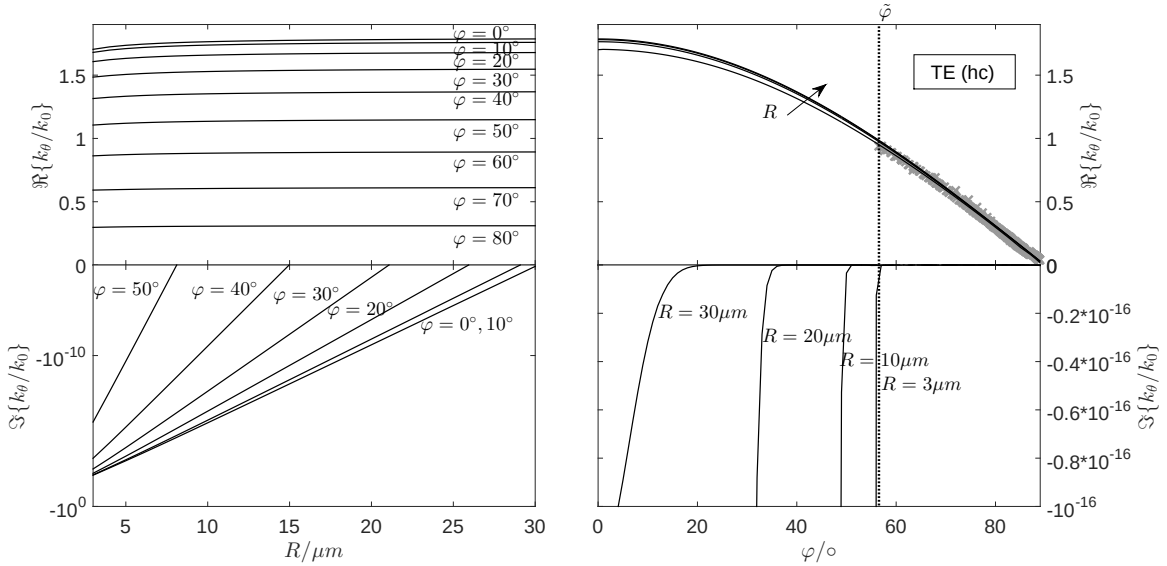

Figure 6: Spiral mode wavenumbers k_θ, real & imaginary parts, for high refractive index contrast (cf. Table 1) and TE-like fields, as a function of bend radius R and angle of incidence φ; critical angle $\tilde{\varphi} = 56.54°$.

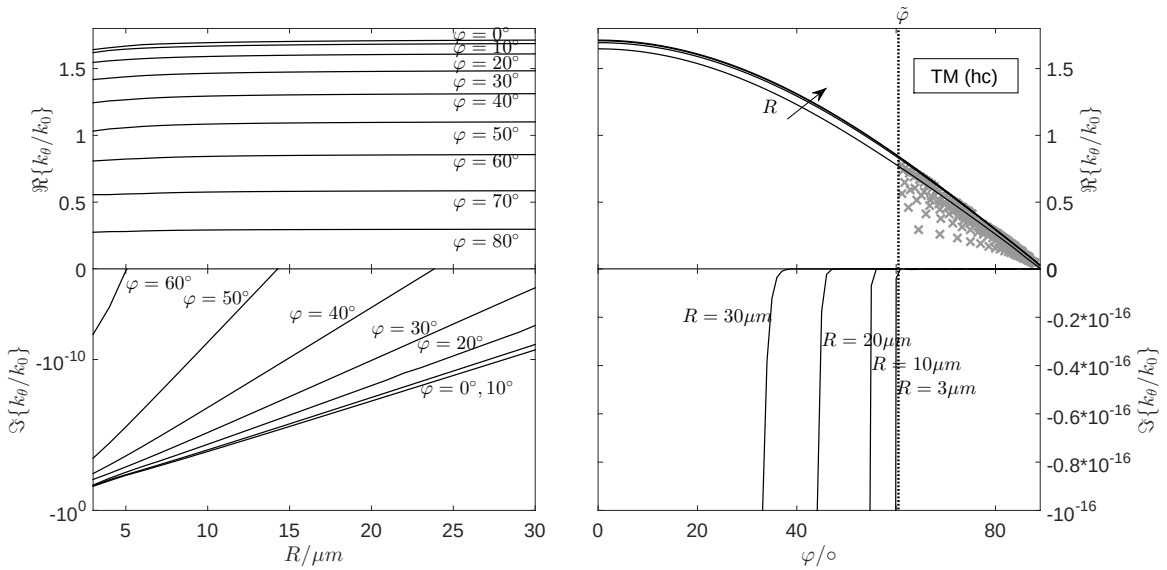

Figure 7: Spiral mode wavenumbers k_θ, real & imaginary parts, for high refractive index contrast (cf. Table 1) and TM-like fields, as a function of bend radius R and angle of incidence φ; critical angle $\tilde{\varphi} = 60.46°$.

of Figures 4–7, for large R, and the limiting cosine-shape of the $\Re\, k_\theta$-curves in the panels on the right. On the scale of the figures, only small deviations from these values for oblique waves in straight slabs are observed, most pronounced for bends with strong curvature at small radii. For the purpose of a more intuitive discussion, we thus accept the "auxiliary" angle φ, introduced to specify the axial wavenumber parameter k_y, as a good approximation of the actual propagation angle φ' of the spiral modes, as defined in Section 2.1.1.

The negative imaginary parts of k_θ represent the attenuation of the spiral modes. With the exception of the configurations with the strongest curvature, at small R, we observe a logarithmic dependence of these attenuation constants on the bend radius, just as for the former bend modes. The losses reduce drastically with increasing propagation angle; this effect becomes more striking when considering the linear plots of attenuation constants versus propagation angle: Attenuation may drop below some tiny admissible upper limit even at angles well below the critical angle $\tilde{\varphi}$, introduced in Section 2.3. In line with the theory, radiative losses vanish entirely, $\Im\, k_\theta = 0$, for propagation at angles $\varphi > \tilde{\varphi}$. Gray markers in the respective region represent discrete solutions for the guided modes of full tubes as introduced in Section 2.3; examples will be discussed in Section 3.3.

We observe the same qualitative behaviour for TE- and TM-like polarized waves, and for both our settings with lower and higher refractive index contrast. While there are only minor differences, on the scale of the figures, between waves of both polarizations for the low contrast configurations (Figures 4, 5), these are more

pronounced for higher refractive index contrast (Figures 6, 7). Quantitatively, however, there is a pronounced difference between the results for different refractive index contrasts, with substantially higher loss levels for the (hc)-configurations,

A few examples for the radial profiles of spiral modes are shown in 8, for TE-like modes supported by our low-contrast bends; the profiles are normalized according to Eq. (12). Note that the plots of Figure 3(a) could be grouped into this series. Figures 9, 10 illustrate field pattern associated with the propagation of the spiral modes, for small bend radii. The plots relate to the electric field component $E_\perp = -\sin(\varphi)E_\theta + \cos(\varphi)E_y$ that is perpendicular to the local "in-plane" wavevector (k_θ, k_y), and to the energy density $w = \frac{1}{4}(\epsilon_0\epsilon|\boldsymbol{E}|^2 + \mu_0|\boldsymbol{H}|^2)$ associated with the spiral mode field.

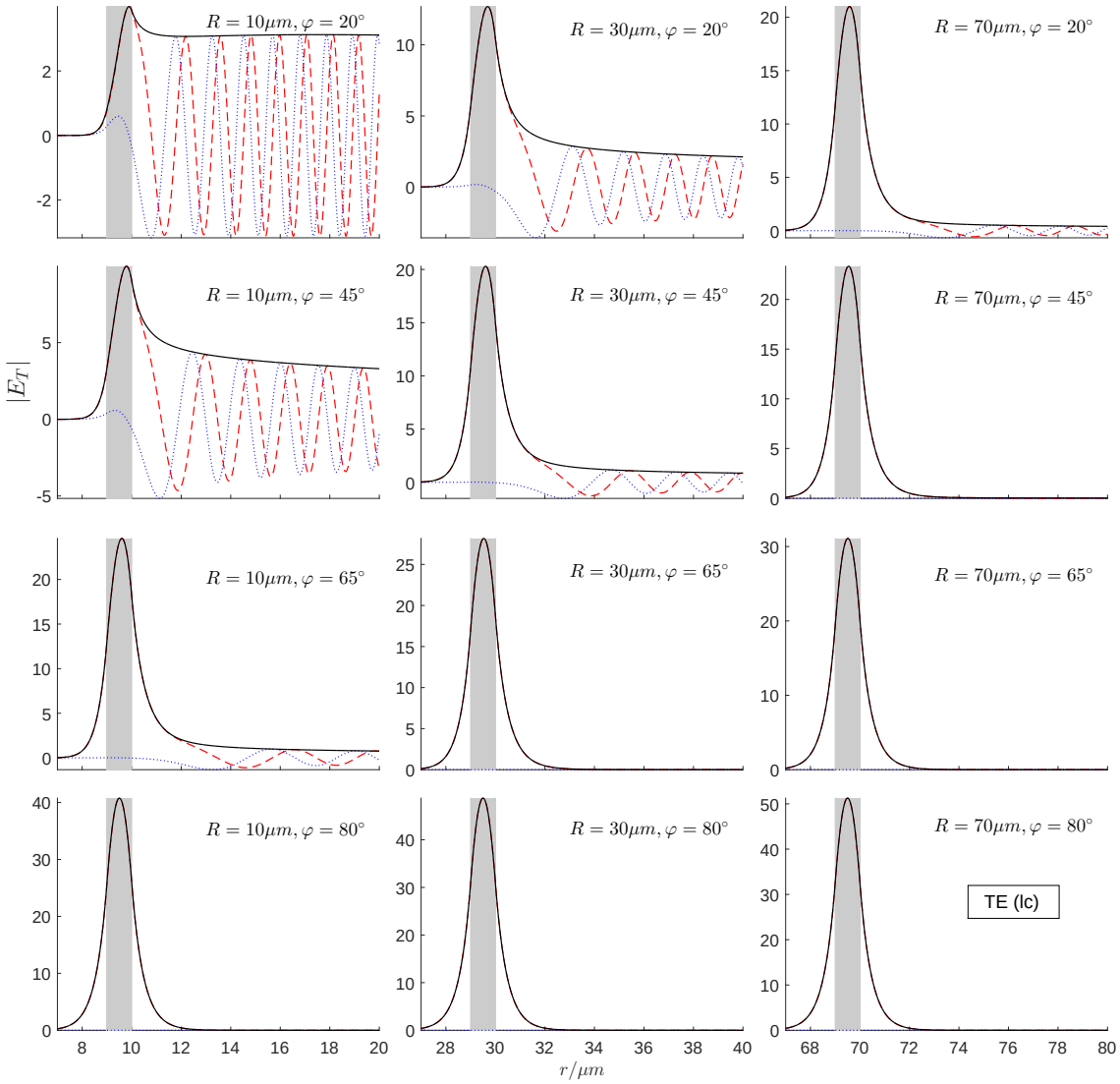

Figure 8: Normalized radial profiles of TE-like spiral modes, for configurations with lower refractive index contrast, for a series of bend radii R and propagation angles φ, parameters as in Table 1. The curves correspond to the absolute value (continuous line), the real part (dashed), and the imaginary part (dotted) of the in-plane electric field component $E_\perp$ that is perpendicular to the direction of propagation.

According to Figure 8, the previously observed lower losses for increased bend radius, or alternatively, for increased angle of propagation, are accompanied by less pronounced external oscillatory tails of the mode profiles. Simultaneously the mode profile maximum shifts inwards. For the lossless configurations, at $\varphi = 80°$ ($\varphi > \tilde{\varphi}$), and irrespective of R, the profiles resemble (these are still Bessel functions, piecewise) the symmetric shapes associated with the fundamental TE modes of straight slab waveguides. Apparently, spiral modes at larger angles of propagation experience a lower "effective curvature", and correspondingly show less of the effects associated with waveguide bending.

This notion is also supported by the field pattern of Figures 9, 10. Note that among the configurations of Figures 4, 6, this concerns the bend slabs with the smallest radii. The plots show the wave propagation guided by the bend core, with a gradual decay in field strength, and with radiated fields outside the bend. The propaga-

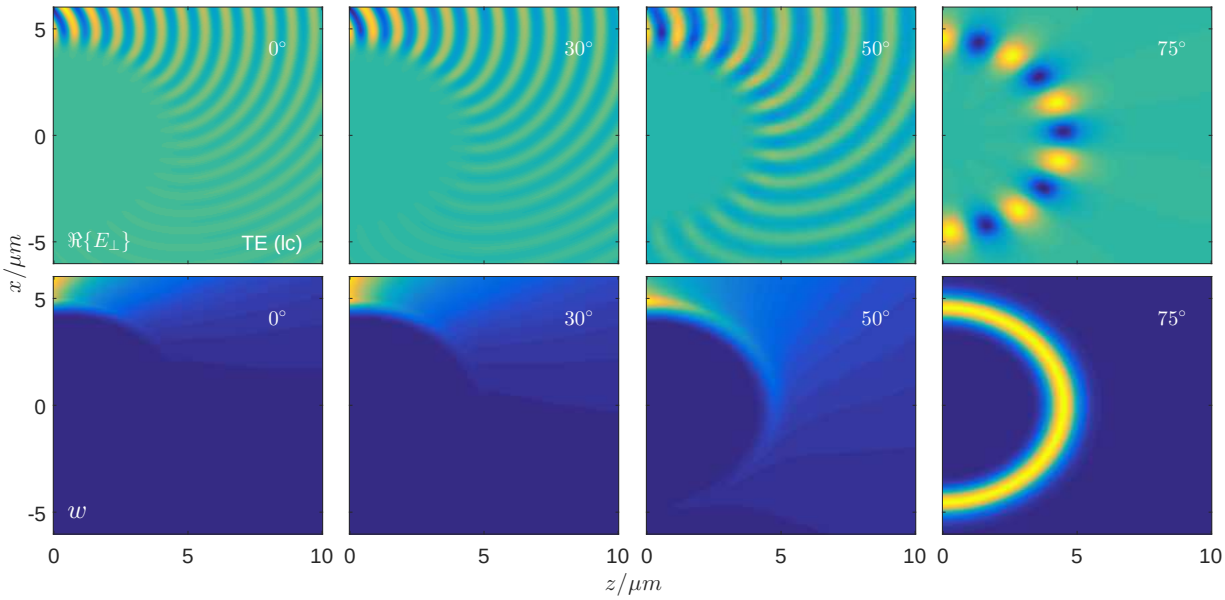

Figure 9: Snapshots of transverse electric fields $\Re\, E_\perp$ (top) and pattern of optical energy density w (bottom) for TE-like spiral modes of a low-contrast bend with radius $R = 5\mu m$, at different angles of propagation φ, for the parameters of Table 1.

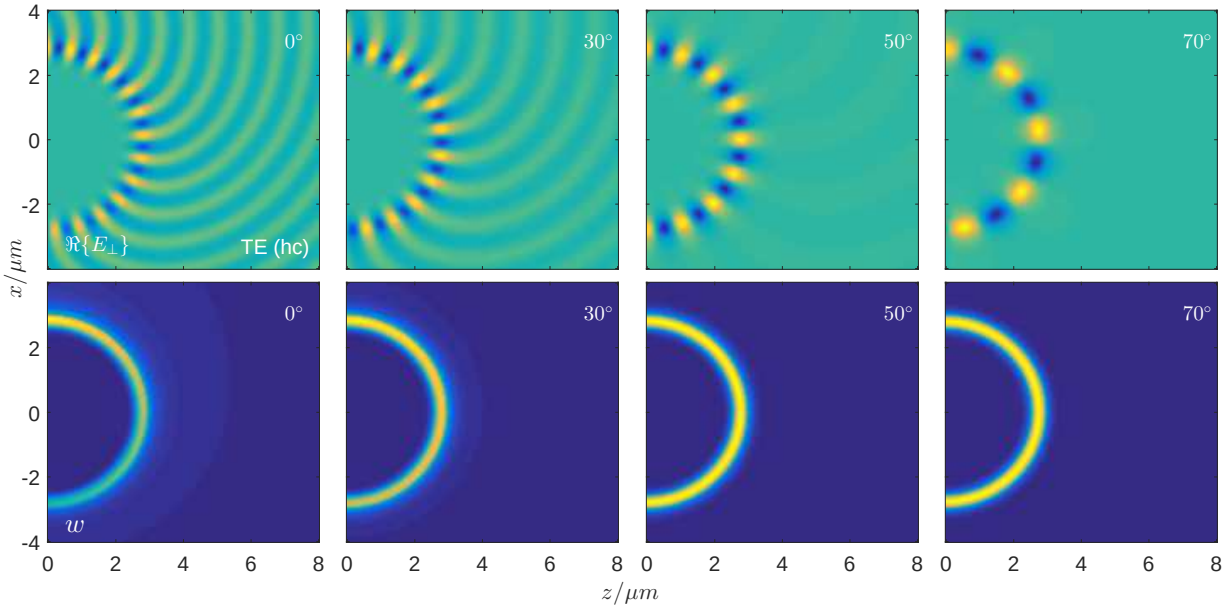

Figure 10: Snapshots of transverse electric fields $\Re\, E_\perp$ (top) and pattern of optical energy density w (bottom) for TE-like spiral modes supported by a high-contrast bend with radius $R = 3\mu m$, at different angles of propagation φ, for the parameters of Table 1.

tion length, the angular distance before loosing specific amounts of power, increases with larger propagation angles; simultaneously the field becomes more and more confined to the core. Spiral modes at angles beyond $\tilde{\varphi}$ propagate along the curved slab with constant amplitude, without radiating optical power into the external region.

While so far things appear, more or less, just as observed for the "standard", scalar 2-D bend modes, we'd like to point out that this concerns hybrid, vectorial modal fields. To characterize the polarization character of the spiral modes, we consider the relative strength

$$\Gamma_{\mathrm{E}} = \int_0^\infty |E_\perp|^2 \mathrm{d}r \Big/ \int_0^\infty |\boldsymbol{E}|^2 \mathrm{d}r \tag{13}$$

of the in-plane electric field component $E_\perp$ perpendicular to the local wavevector. In case of a straight slab waveguide, the ratio (13) identifies the modal polarization through values of 1 for 2-D TE slab modes, and 0 for the TM modes. Figure 11 summarizes polarization ratios for our spiral modes.

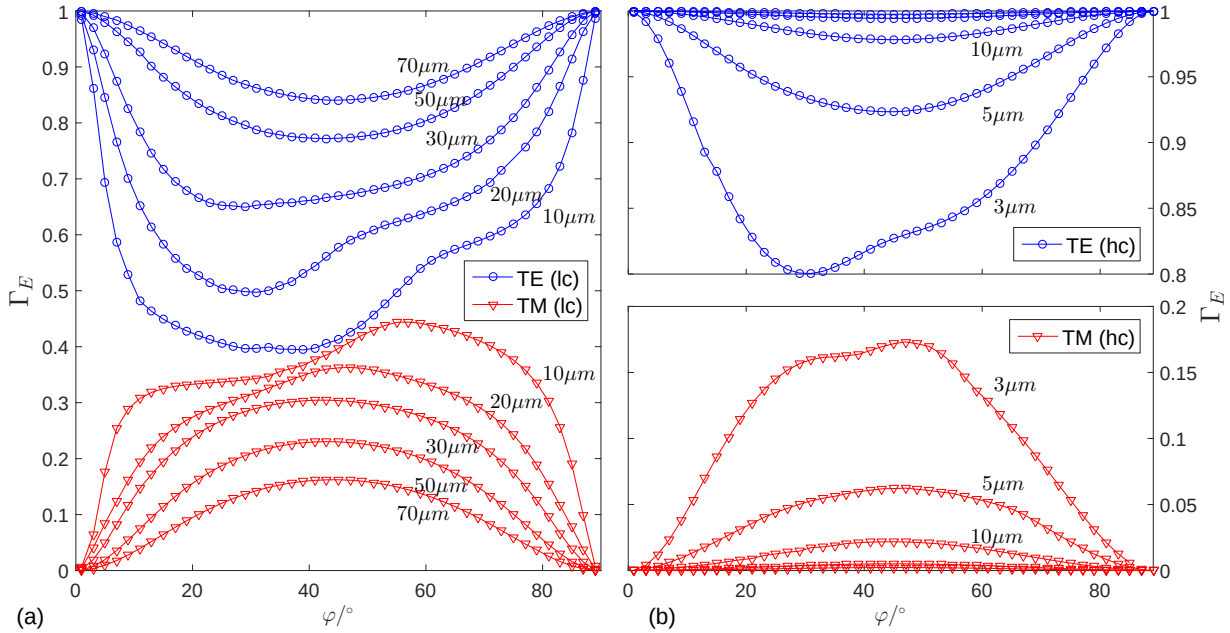

Figure 11: Polarization ratios Γ_E, as defined in Eq. (13), for spiral modes with low (a) and high refractive index contrast (b), for bends (cf. Table 1) with different radii R, as a function of the propagation angle φ.

At angle $\varphi = 0$, problems split exactly into scalar TE- and TM- bend modes, for arbitrary radii; one observes values Γ_E near to 1 and 0 also for spiral modes with close by parameters. For larger, intermediate angles the modes become more hybrid. This feature is more pronounced for strong curvature bends with smaller radii. For larger propagation angles, the reduced effective curvature experienced by the propagating waves leads again to spiral modes with distinct polarization. Comparison of panels (a) and (b) of Figure 11 shows that the higher refractive index contrast, with correspondingly stronger mode confinement, appears to suppress partly the large hybridization, such that, at intermediate angles, the polarization character of the spiral modes remains even closer to the states for $\varphi = 0^\circ, \approx 90^\circ$. With hindsight, these findings justify the classification of solutions into TE- and TM-like spiral modes, as applied throughout this paper.

For specific configurations at intermediate propagation angles, and for high curvature, only the link through continuous parameter changes to the respective structures at $\varphi = 0$ motivates the classification of the pronouncedly hybrid spiral modes. We therefore take a closer look at a pair of such modes. Figure 12 compares normalized vectorial electric field profiles of spiral modes at $\varphi \approx 45^\circ$, for a low contrast bend at $R = 10\,\mu$m radius.

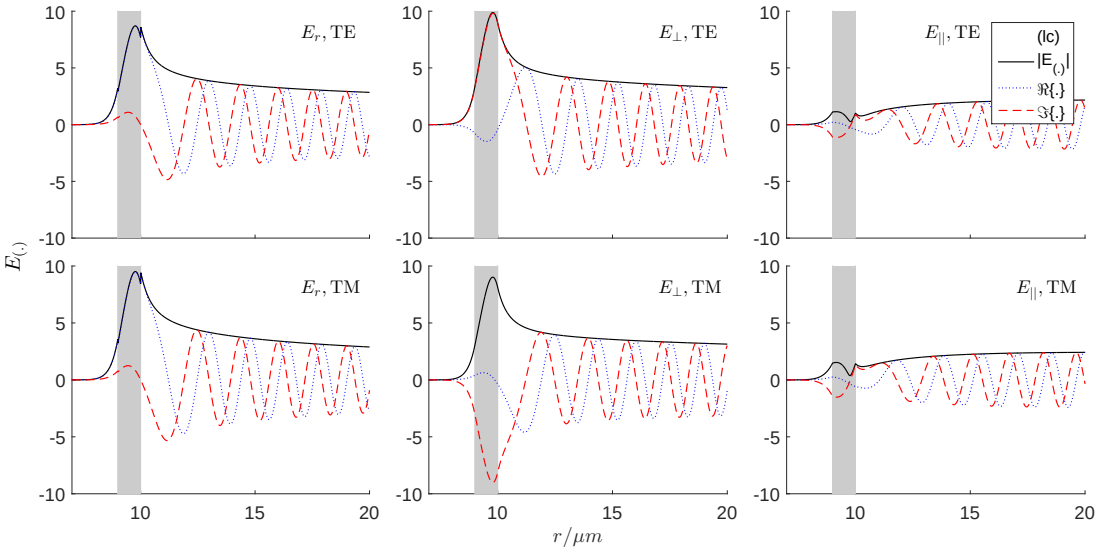

Figure 12: Electric profiles of TE- and TM-like hybrid spiral modes supported by a low-contrast bend (cf.Table 1) of radius $R = 10\,\mu$m. These are modes with equal k_y, given by angles $\varphi = 45.0^\circ$ (TE) and $\varphi = 45.1^\circ$ (TM). The curves show the absolute value (continuous), the real part (dotted), and the imaginary part (dashed) of the electric components in radial direction E_r, and in-plane in directions perpendicular $E_\perp$ and parallel $E_\parallel$ to the direction of propagation.

In addition to the radial component E_r, and the in-plane transverse component $E_\perp$, also the longitudinal electric component $E_\parallel = \cos(\varphi)E_\theta + \sin(\varphi)E_y$ parallel to the local "in-plane" wavevector (k_θ, k_y) was considered for Figure 12. The fields still resemble the major electric components of their "original" (straight slab) TE- and TM-shapes, only that both spiral modes exhibit strong fields E_r and $E_\perp$ in *both* transversal directions. The modes differ (and are possibly orthogonal [2], in a suitable sense) in the relative signs of these large transverse electric profile components.

3.3 Tube modes

We now consider specifically the lossless waves in the region $\varphi > \tilde{\varphi}$ of large propagation angles. Imagine the former bend segments being extended towards entire circular cylinders, for angular range $\theta \in [0, 2\pi]$. We then look at circular dielectric fibers with specific, piecewise-constant single layer refractive index profiles. As argued in Section 2.3, with small modifications our previous theory can be applied to determine the guided modes supported by these tube-shaped optical fibers. The axial wavenumber, the propagation constant of these tube modes, is now being sought as the eigenvalue of the modal eigen-problem, for given integer angular order $\nu = k_\theta R \in \mathbb{Z}$. Respective results are collected in Figure 13.

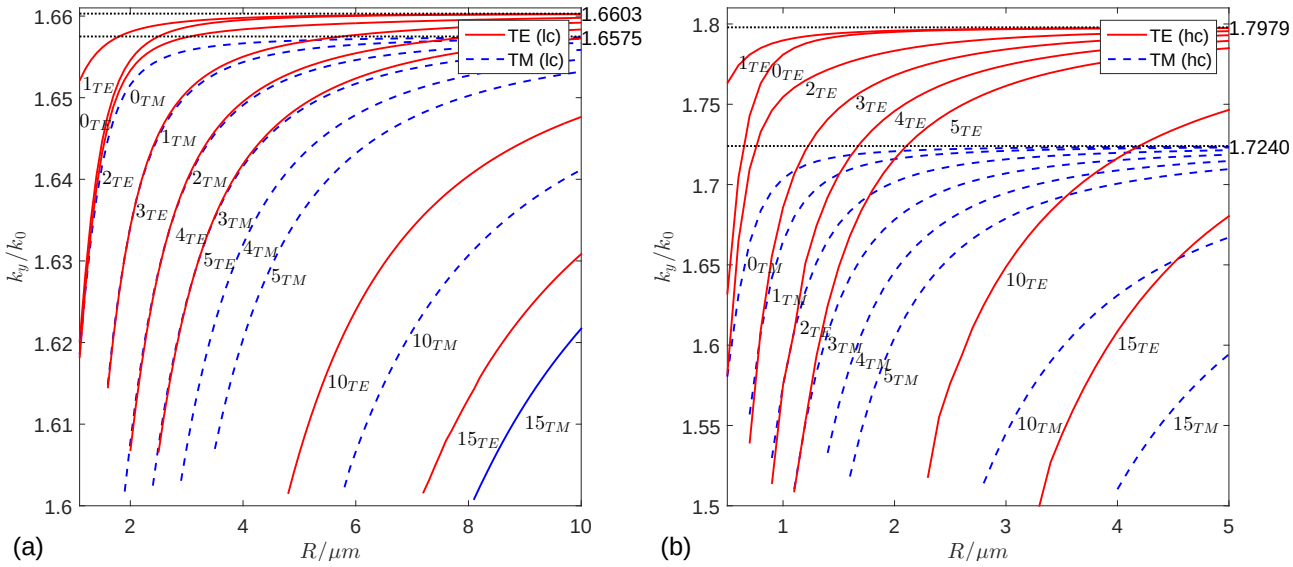

Figure 13: Effective indices k_y/k_0 of polarized tube modes versus the outer radius R of the tube, for mode orders $\nu = k_\theta R$ between 0 and 15 (not all are shown). Structures with lower (a) and higher refractive index contrast (b) are considered, with parameters as in Table 1. Horizontal lines indicate the effective indices of polarized modes of straight slab waveguides [19] with equivalent parameters.

For TE-like polarization, the modes of first angular order, rather than those of zeroth order, appear as fundamental modes, with the highest propagation constants. This corresponds to respective observations [17, 18] for standard step-index optical fibers, where the TE_{01}- and TM_{01}-modes (LP_{11}), of angular order 0, i.e. with constant angular functions, have effective indices below those of the fundamental HE_{11}-mode (LP_{01}).

At fixed mode order ν, and for large tube radii, the in-plane wavevectors $(k_y, k_\theta = \nu/R)$ of the tube modes tend towards the axial direction. Also, for large radii, the waves are guided by a refractive index profile with lower and lower curvature, that becomes eventually similar to that of a straight slab waveguide. Therefore, in the limit of large tube radii, the effective indices of the tube modes are seen to converge to the effective indices of these straight slab waveguides.

Reasoning that the discrete tube fields are just special cases of our former spiral modes, in the range of vanishing losses $\varphi > \tilde{\varphi}$, and for "accidentally" integer angular order, these are to be compared with the previous findings for the spiral modes of angular segments of these tubes. To that end, the given modal orders ν, and the k_y-eigenvalues that represent the tube modes in Figure 13 are translated to wavenumbers $k_\theta = \nu/R$ and propagation angles φ, with $\sin\varphi = k_y/(k_0 N_{\text{eff}})$, that characterize the constituting spiral modes. Figure 14 shows an enlargement of Figures 4–7, for the range beyond $\tilde{\varphi}$. Wavenumbers for the spiral modes match those associated with the discrete tube modes for equal radius and polarization. This comparison can serve as a test of consistency for the two different computational procedures (cf. Section 2.3) that led to the data.

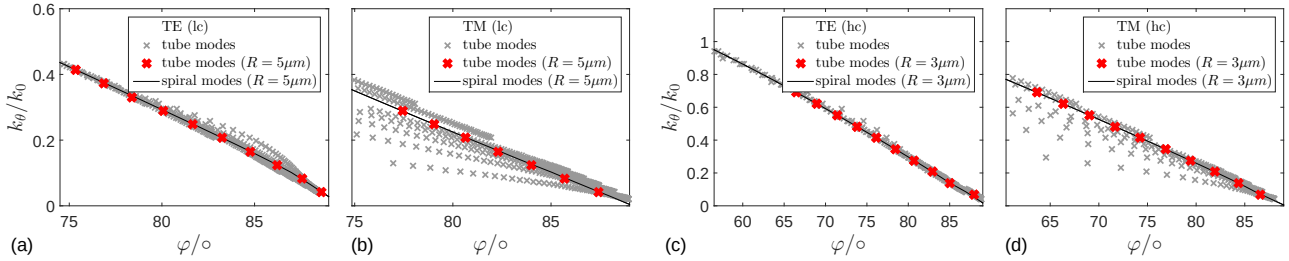

Figure 14: Angular wavenumbers k_θ of spiral modes, versus propagation angle φ, and respective data associated with the tube modes, for tube segments / tubes with low refractive index contrast (a, b) and high contrast (c, d); cf. Table 1. The plots show enlargements of Figures 4 – 7, for $\varphi > \tilde{\varphi}$. Panels (a, c) concern TE-like fields, while panels (b, d) relate to TM-like polarization. Gray markers show the wavenumbers associated with all tube modes of Figure 13, while the lines and the red, bold-face markers concern wavenumbers for tube radii $R = 5\ \mu$m (a, b) and $R = 3\ \mu$m (c, d).

Finally, Figure 15 gives an impression of the field shapes associated with modes of angular order $\nu = 8$, for tubes of both levels of refractive index contrast, and for the small radii that were also considered for Figures 9, 10. These fields can be viewed as being constructed from spiral modes with propagation angles of $\varphi = 78.6°$ (low contrast, Figure 15(a)) and $\varphi = 71.4°$ (high contrast, Figure 15(b)). Note the remarks on the degeneracy of the tube modes in Section 2.3.

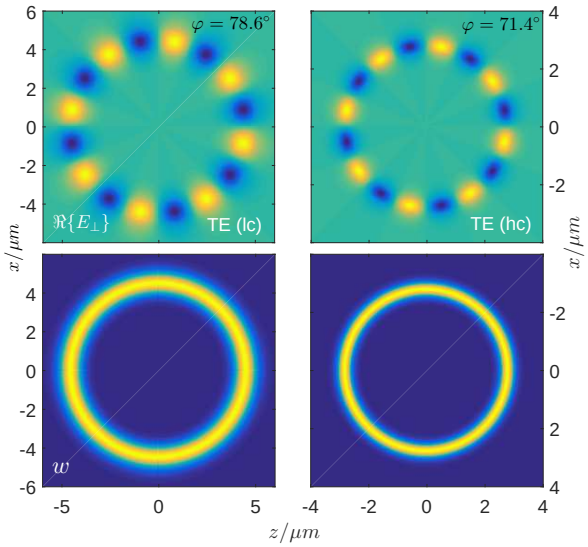

Figure 15: Transverse electric fields $E_\perp$, and electromagnetic energy density w, of TE-like tube modes of angular order $\nu = 8$, for tube structures (see Table 1) of low (a) and high refractive index contrast (b), with radii of $R = 5\ \mu$m (a) and $R = 3\ \mu$m (b).

4 Concluding remarks

For oblique angles of wave propagation relative to the symmetry axis, bent dielectric slabs support a continuum of vectorial quasi-guided spiral modes, that can be parameterized by the axial wavenumber component. Our analytical formalism covers standard bend modes, spiral modes for varying angles of propagation, and lossless waves at near-axis angles that constitute the guided modes of the full dielectric tubes.

Polarized scalar TE- and TM-bend modes correspond to zero axial wavenumber, or to zero propagation angle, respectively. Starting from these, the vectorial spiral modes at larger angles of propagation experience a lower "effective curvature", with reduced radiative losses and correspondingly smaller exterior field strengths, and their field maxima appear at smaller radial positions. Radiative losses vanish altogether for propagation angles beyond a critical limit, given by the wavenumber associated with plane waves in the exterior medium. Guided tube modes can be associated with specific discrete spiral waves beyond this critical angle.

Effective indices and attenuation constants of spiral modes have been calculated, and field profiles illustrated, for sets of parameters with different refractive index contrast. While the modal confinement grows with the index contrast, such that the effects of the curvature are seen at smaller bend radii, the phenomenon of vanishing radiative losses becomes the more dramatic for the low-contrast configurations. Also here, our formalism predicts low losses (compared to the standard 2-D bend) for quite small radii, even for spiral modes at propagation angles below the critical limit.

A Continuity of spiral mode profiles

We refer to the bend configuration as introduced in Figure 1, and the formalism of Sections 2.1–2.1.2. Principal field components E_y and H_y are defined piecewise for the regions $r < R - d$, $R - d < r < R$, and $R < r$ in the form of Eq. (8), with separate coefficients A_E, B_E, C_E, D_E, and A_H, B_H, C_H, D_H, respectively. Eqs. (5) relate the principal fields to the remaining electromagnetic components E_θ, H_θ, E_r, and H_r.

Requiring the principal components E_y and H_y, and the angular components E_θ and H_θ, to be continuous at $r = R^- = R - d$ leads to the equations

$$A_E \mathrm{J}_\nu(R^-\chi_\mathrm{s}) = B_E \mathrm{J}_\nu(R^-\chi_\mathrm{f}) + C_E \mathrm{Y}_\nu(R^-\chi_\mathrm{f}), \tag{14}$$

$$A_H \mathrm{J}_\nu(R^-\chi_\mathrm{s}) = B_H \mathrm{J}_\nu(R^-\chi_\mathrm{f}) + C_H \mathrm{Y}_\nu(R^-\chi_\mathrm{f}), \tag{15}$$

$$\begin{aligned} &\frac{1}{\chi_\mathrm{s}^2}\Big(-\mathrm{i}\frac{k_y\nu}{R^-} A_E \mathrm{J}_\nu(R^-\chi_\mathrm{s}) - \omega\mu_0\chi_\mathrm{s} A_H \mathrm{J'}_\nu(R^-\chi_\mathrm{s})\Big) \qquad (16)\\ = \;& \frac{1}{\chi_\mathrm{f}^2}\Big(-\mathrm{i}\frac{k_y\nu}{R^-}\left(B_E \mathrm{J}_\nu(R^-\chi_\mathrm{f}) + C_E \mathrm{Y}_\nu(R^-\chi_\mathrm{f})\right) - \omega\mu_0\chi_\mathrm{f}\left(B_H \mathrm{J'}_\nu(R^-\chi_\mathrm{f}) + C_H \mathrm{Y'}_\nu(R^-\chi_\mathrm{f})\right)\Big), \end{aligned}$$

$$\begin{aligned} &\frac{1}{\chi_\mathrm{s}^2}\Big(-\mathrm{i}\frac{k_y\nu}{R^-} A_H \mathrm{J}_\nu(R^-\chi_\mathrm{s}) + \omega\epsilon_0 n_\mathrm{s}^2\chi_\mathrm{s} A_E \mathrm{J'}_\nu(R^-\chi_\mathrm{s})\Big) \qquad (17)\\ = \;& \frac{1}{\chi_\mathrm{f}^2}\Big(-\mathrm{i}\frac{k_y\nu}{R^-}\left(B_H \mathrm{J}_\nu(R^-\chi_\mathrm{f}) + C_H \mathrm{Y}_\nu(R^-\chi_\mathrm{f})\right) + \omega\epsilon_0 n_\mathrm{f}^2\chi_f\left(B_E \mathrm{J'}_\nu(R^-\chi_\mathrm{f}) + C_E \mathrm{Y'}_\nu(R^-\chi_\mathrm{f})\right)\Big). \end{aligned}$$

Likewise, these four fields are continuous at the outer interface at $r = R$, if the equations

$$B_E \mathrm{J}_\nu(R\chi_\mathrm{f}) + C_E \mathrm{Y}_\nu(R\chi_\mathrm{f}) = D_E \mathrm{H}_\nu^{(2)}(\pm R\chi_\mathrm{c}), \tag{18}$$

$$B_H \mathrm{J}_\nu(R\chi_\mathrm{f}) + C_H \mathrm{Y}_\nu(R\chi_\mathrm{f}) = D_H \mathrm{H}_\nu^{(2)}(\pm R\chi_\mathrm{c}), \tag{19}$$

$$\begin{aligned} &\frac{1}{\chi_\mathrm{f}^2}\Big(-\mathrm{i}\frac{k_y\nu}{R}\left(B_E \mathrm{J}_\nu(R\chi_\mathrm{f}) + C_E \mathrm{Y}_\nu(R\chi_\mathrm{f})\right) - \omega\mu_0\chi_\mathrm{f}\left(B_H \mathrm{J'}_\nu(R\chi_\mathrm{f}) + C_H \mathrm{Y'}_\nu(R\chi_\mathrm{f})\right)\Big)\\ = \;& \frac{1}{\chi_\mathrm{c}^2}\Big(-\mathrm{i}\frac{k_y\nu}{R} D_E \mathrm{H}_\nu^{(2)}(\pm R\chi_\mathrm{c}) \mp \omega\mu_0\chi_\mathrm{c} D_H \mathrm{H}_\nu^{(2)'}(\pm R\chi_\mathrm{c})\Big), \qquad (20) \end{aligned}$$

$$\begin{aligned} &\frac{1}{\chi_\mathrm{f}^2}\Big(-\mathrm{i}\frac{k_y\nu}{R}\left(B_H \mathrm{J}_\nu(R\chi_\mathrm{f}) + C_H \mathrm{Y}_\nu(R\chi_\mathrm{f})\right) + \omega\epsilon_0 n_\mathrm{f}^2\chi_\mathrm{f}\left(B_E \mathrm{J'}_\nu(R\chi_\mathrm{f}) + C_E \mathrm{Y'}_\nu(R\chi_\mathrm{f})\right)\Big)\\ = \;& \frac{1}{\chi_\mathrm{c}^2}\Big(-\mathrm{i}\frac{k_y\nu}{R} D_H \mathrm{H}_\nu^{(2)}(\pm R\chi_\mathrm{c}) \pm \omega\epsilon_0 n_\mathrm{c}^2\chi_\mathrm{c} D_E \mathrm{H}_\nu^{(2)'}(\pm R\chi_\mathrm{c})\Big) \qquad (21) \end{aligned}$$

are satisfied. Here abbreviations $\chi_r = \sqrt{k_0^2 n_r^2 - k_y^2}$, for $r \in \{\mathrm{s}, \mathrm{f}, \mathrm{c}\}$, have been introduced. Signs $\pm$ and $\mp$ distinguish wavenumber parameters $k_y \lessgtr k_0 n_\mathrm{c}$. Just as in the discussion of Eq. (8), the $\sqrt{\ }$-symbol is meant to indicate the positive real root, for a positive radicand, or the imaginary root with positive imaginary part, in case of a negative radicand. Eqs. (14)–(21) imply continuity of H_r and of $n^2 E_r$ at the radial positions of both interfaces.

Acknowledgments

Financial support from the German Research Foundation (Deutsche Forschungsgemeinschaft DFG, projects HA 7314/1-1, GRK 1464, and TRR 142) is gratefully acknowledged.

References

[1] C. Vassallo. *Optical Waveguide Concepts*. Elsevier, Amsterdam, 1991.

[2] K. R. Hiremath, M. Hammer, R. Stoffer, L. Prkna, and J. Čtyroký. Analytical approach to dielectric optical bent slab waveguides. *Optical and Quantum Electronics*, 37(1-3):37–61, 2005.

[3] M. Hammer. Oblique incidence of semi-guided waves on rectangular slab waveguide discontinuities: A vectorial QUEP solver. *Optics Communications*, 338:447–456, 2015.

[4] M. Hammer, A. Hildebrandt, and J. Förstner. How planar optical waves can be made to climb dielectric steps. *Optics Letters*, 40(16):3711–3714, 2015.

[5] M. Hammer, A. Hildebrandt, and J. Förstner. Full resonant transmission of semi-guided planar waves through slab waveguide steps at oblique incidence. *Journal of Lightwave Technology*, 34(3):997–1005, 2016.

[6] P. K. Tien. Integrated optics and new wave phenomena in optical waveguides. *Reviews of Modern Physics*, 49(2):361–419, 1977.

[7] R. Ulrich and R. J. Martin. Geometrical optics in thin film light guides. *Applied Optics*, 10(9):2077–2085, 1971.

[8] *Maple 2016* technical computing software. https://www.maplesoft.com/products/maple/.

[9] M. K. Chin, D. Y. Chu, and S.-T. Ho. Estimation of the spontaneous emission factor for microdisk lasers via the approximation of whispering gallery modes. *Journal of Applied Physics*, 75(7):3302–3307, 1994.

[10] J. A. Lock. Morphology-dependent resonances of an infinitely long circular cylinder illuminated by a diagonally incident plane wave or a focused gaussian beam. *Journal of the Optical Society of America A*, 14(3):653–661, 1997.

[11] H. G. L. Schwefel, Stone A. D., and H. E. Tureci. Polarization properties and dispersion relations for spiral resonances of a dielectric rod. *Journal of the Optical Society of America B*, 22(11):2295–2307, 2005.

[12] A. W. Poon, R. K. Chang, and J. A. Lock. Spiral morphology-dependent resonances in an optical fiber: effects of fiber tilt and focused Gaussian beam illumination. *Optics Letters*, 23(14):1105–1107, 1998.

[13] T. A. Birks, J. C. Knight, and T. E. Dimmick. High-resolution measurement of the fiber diameter variations using whispering gallery modes and no optical alignment. *IEEE Photonics Technology Letters*, 12(2):182–183, 2000.

[14] J. D. Jackson. *Classical Electrodynamics, 3rd. ed.* Wiley, New York, 1998.

[15] M. Abramowitz and I. A. Stegun. *Handbook of Mathematical Functions*. National Bureau of Standards, Washington, D.C., 1964.

[16] W. H. Press, S. A. Teukolsky, W. T. Vetterling, and B. P. Flannery. *Numerical Recipes in C, 2nd ed.* Cambridge University Press, 1992.

[17] A. W. Snyder and J. D. Love. *Optical Waveguide Theory*. Chapman and Hall, London, New York, 1983.

[18] K. Okamoto. *Fundamentals of Optical Waveguides*. Academic Press, SanDiego, 2000.

[19] M. Hammer. OMS — 1-D mode solver for dielectric multilayer slab waveguides. http://www.computational-photonics.eu/oms.html.